

Integrated flexible microwave device for magnetic material scanning using nitrogen-vacancy center

Xiaoyu Xing(邢潇玉), Jingqiang Han(韩敬强), Wentao Lu(卢文韬), Zhiqiang Zhang(张致强), Yang Wang(汪洋), Shu Liu(刘澍), Na Li(李娜), Yinjun Wang(王银君), Ziyan Wu(吴紫妍), Xinyu Liu(刘心宇), Shengkai Xia(夏圣开), Keqi Shi(施柯琦), Bo Yang(杨博), Chenlu Bu(步晨露), Guanxiang Du(杜关祥)

Citation: Chin. Phys. B. 35, 094215 (2026).DOI: 10.1088/1674-1056/ae6f97| CSTR: 32038.14.CPB.ae6f97
http://cpb.iphy.ac.cn; http://iopscience.iop.org/cpb

What follows is a list of articles you may be interested in

Diamond NV center quantum magnetic sensor using a dual-frequency broadband antenna

Ke-Qi Shi(施柯琦), Heng Hang(杭衡), Wen-Tao Lu(卢文韬), Jing-Cheng Huang(黄竟成), Na Li(李娜), Jin-Xu Wang(王金旭), Zeng-Bo Xu(许增博), Lin-Yan Yu(虞林嫣), Sheng-Kai Xia(夏圣开), Yu-Chen Bian(卞雨辰), Guan-Xiang Du(杜关祥)

Chin. Phys. B. 34, 094205 (2025). DOI: 10.1088/1674-1056/add900 | CSTR: 32038.14.CPB.add900

Design of compact integrated diamond nitrogen–vacancy center quantum probe

Sheng-Kai Xia(夏圣开), Wen-Tao Lu(卢文韬), Xu-Tong Zhao(赵旭彤), Ya-Wen Xue(薛雅文), Zeng-Bo Xu(许增博), Shi-Yu Ge(葛仕宇), Yang Wang(汪洋), Lin-Yan Yu(虞林嫣), Yu-Chen Bian(卞雨辰), Si-Han An(安思瀚), Bo Yang(杨博), Jian-Jun Xiang(向建军), Guan-Xiang Du(杜关祥)

Chin. Phys. B. 33, 054202 (2024). DOI: 10.1088/1674-1056/ad2bf6

Design of tightly linked dual ring antenna and imaging of magnetic field distribution using a diamond fiber probe

Qing-Yun Ye(叶青云), Ya-Wen Xue(薛雅文), Fei-Yue He(何飞越), Xu-Tong Zhao(赵旭彤), Yu-Chen Bian(卞雨辰), Wen-Tao Lu(卢文韬), Jin-Xu Wang(王金旭), Hong-Hao Chen(陈鸿浩), Sheng-Kai Xia(夏圣开), Ming-Jing Zeng(曾明菁), Guan-Xiang Du(杜关祥)

Chin. Phys. B. 33, 024202 (2024). DOI: 10.1088/1674-1056/ad0772

A novel demodulation method for transmission using nitrogen-vacancy-based solid-state quantum sensor

Ruixin Bai(白瑞昕), Xinyue Zhu(朱欣岳), Fan Yang(杨帆), Tianran Gao(高天然), Ziran Wang(汪子然), Linyan Yu(虞林嫣), Jinfeng Wang(汪晋锋), Li Zhou(周力), Guanxiang Du(杜关祥)

Chin. Phys. B. 31, 074203 (2022). DOI: 10.1088/1674-1056/ac5618

Light slowing and all-optical time division multiplexing of hybrid four-wave mixing signal in nitrogen-vacancy center

Ruimin Wang(王瑞敏), Irfan Ahmed, Faizan Raza, Changbiao Li(李昌彪), Yanpeng Zhang(张彦鹏)

Chin. Phys. B. 29, 054204 (2020). DOI: 10.1088/1674-1056/ab7b50

Integrated flexible microwave device for magnetic material scanning using nitrogen-vacancy center

Xiao-Yu Xing(邢潇玉)[1], Jing-Qiang Han(韩敬强)[1], Wen-Tao Lu(卢文韬)[1], Zhi-Qiang Zhang(张致强)[1], Yang Wang(汪洋)[2], Shu Liu(刘澍)[1], Na Li(李娜)[1], Yin-Jun Wang(王银君)[3], Zi-Yan Wu(吴紫妍)[3], Xin-Yu Liu(刘心宇)[3], Sheng-Kai Xia(夏圣开)[4], Ke-Qi Shi(施柯琦)[1], Bo Yang(杨博)[5], Chen-Lu Bu(步晨露)[1], and Guan-Xiang Du(杜关祥)[1,†]

[1] *College of Telecommunications and Information Engineering, Nanjing University of Posts and Telecommunications, Nanjing* 210003, *China*
[2] *School of Science, Nanjing University of Posts and Telecommunications, Nanjing* 210023, *China*
[3] *School of Electronic and Optical Engineering, Nanjing University of Posts and Telecommunications, Nanjing* 210023, *China*
[4] *School of Computer Science, Nanjing University of Posts and Telecommunications, Nanjing* 210023, *China*
[5] *School of Electronic and Information Engineering, Nanjing Vocational Institute of Transport Technology, Nanjing* 211188, *China*

(Received 12 March 2026; revised manuscript received 17 April 2026; accepted manuscript online 19 May 2026)

We design a flexible microwave transmission line based on a splitting-combining structure and integrate it with a fiber-diamond probe to form a unified quantum probe, providing a resonant driving microwave magnetic field. This device utilizes a polyimide (PI) flexible substrate, which is conformable. A through-hole is designed at the center of the ring to accommodate fiber insertion, enabling the sensing unit to approach the sample under test. Experimental results demonstrate that the device achieves a 394 MHz bandwidth, with a microwave efficiency of 4.64 G/$\sqrt{\text{W}}$, balancing broadband with a strong near-field microwave magnetic field. Finally, we characterize the spatial distributions of the static magnetic-field magnitude and the angle between the static magnetic field and the selected NV axis on the surface of the kagome magnet $TmMn_6Sn_6$, demonstrating the application potential of the proposed probe for magnetic-material characterization.

Keywords: nitrogen-vacancy (NV) center, conformal device, quantum precision measurement, magnetic material microscopy

PACS: 42.50.Ex, 07.55.Ge, 03.65.Yz

DOI: 10.1088/1674-1056/ae6f97 **CSTR:** 32038.14.CPB.ae6f97

1. Introduction

Nitrogen-vacancy (NV) center in diamond is a common intrinsic lattice defect.[1–3] This defect demonstrates stable optical properties and long coherence times at room temperature, allowing for all-optical spin state initialization and readout.[4,5] As a result, it has become a leading platform for solid-state quantum sensing in the field of quantum precision measurement.

Microwave devices are crucial for achieving precise control of spin states, and their structure and performance strongly affect the microwave-driving capability. Currently, two main types of devices are commonly used: one is resonant structures, such as split-ring resonators[6] and resonant devices;[7] the other is transmission structures, such as microstrip lines[8] and coplanar waveguides.[9] The advantage of resonant structures lies in their ability to concentrate energy effectively during resonance, generating strong near-field microwave magnetic fields at specific frequencies. However, due to their narrow bandwidth, they struggle to adapt to broadband requirements. Transmission lines, on the other hand, offer broader bandwidth but fail to generate an efficient near-field microwave magnetic field. For example, Bayat *et al.*[10] proposed double split-ring resonators that generate a microwave magnetic field of 5.6 Gauss, but with a bandwidth of only 40 MHz. Babashah *et al.*[11] proposed a coplanar waveguide (CPW) coil with a bandwidth of 900 MHz, but it generates only a 1.6 Gauss microwave magnetic field. Xia *et al.*[12] introduced a flexible ring resonator with a microwave magnetic field of 3.5 Gauss and a bandwidth of 140 MHz. Therefore, designing a compact device that balances bandwidth and microwave magnetic field becomes particularly important.

In this paper, we designed a flexible transmission line incorporating a through-hole within a ring-shaped microstrip structure. By integrating a tapered fiber–diamond probe, an integrated quantum probe was formed. The transmission line adopts a splitting–combining configuration and can be conformally mounted on a supporting substrate. Its operating frequency is tuned to approximately 2.87 GHz while maintaining a balance between microwave magnetic-field efficiency and bandwidth. The microwave magnetic field distribution was scanned at a distance of approximately 20 μm above this microwave device, and the axial attenuation characteristics were further analyzed. In addition, scanning measurements were performed on the micro-magnetic material, demonstrating the

†Corresponding author. E-mail: duguanxiang@njupt.edu.cn

© 2026 Chinese Physical Society and IOP Publishing Ltd. All rights, including for text and data mining, AI training, and similar technologies, are reserved.

potential of the proposed probe for static magnetic-field characterization.

2. Basic theory and experimental setup

NV center is a kind of point defect in diamond with C_{3v} symmetry, in which a carbon atom is replaced by a nitrogen atom, and an adjacent lattice site becomes a vacancy, as shown in Fig. 1(a).[13–15] Its Hamiltonian[16] can be expressed as

$$H_{\rm s} = DS_z^2 + E\left(S_x^2 - S_y^2\right) + \gamma_{\rm NV}\boldsymbol{B}\cdot\boldsymbol{S}. \tag{1}$$

Here, $D = 2.87$ GHz represents the axial zero-field splitting (ZFS) parameter, E is the non-axial zero-field splitting parameter, mainly caused by the local stress in the diamond. $\gamma_{\rm NV} = -2.802495$ MHz/Gs is the gyromagnetic ratio of electron spin. $\boldsymbol{S}$ is the spin-1 angular momentum operator, with components S_x, S_y, and S_z.

Figure 1(b) shows the energy levels of the NV center. The negatively charged NV center (NV^-) consists of six electrons, two of which are unpaired, giving rise to the spin-triplet ground state $^3A_2$ and excited state ^3E. Spin–spin interaction results in the zero-field splitting between the $m_{\rm s} = 0$ and $m_{\rm s} = \pm 1$. Without an external static magnetic field, the $m_{\rm s} = \pm 1$ spin states are degenerate, with a ZFS of 2.87 GHz between them and $m_{\rm s} = 0$.[17,18] Pumped by a 532 nm green laser, the system in the ground state absorbs energy and transitions to the excited state, then returns to the ground state through either radiative or non-radiative transitions.

Optically detected magnetic resonance (ODMR) combines optical and microwave resonance techniques, enabling the readout of the NV center's electron spin states through analyzing fluorescence intensity.[19,20] With an axial static magnetic field, the degenerate state $m_{\rm s} = \pm 1$ splits to $m_{\rm s} = +1$ and $m_{\rm s} = -1$, following the Zeeman effect.[21] Energy level transitions between $m_{\rm s} = 0$ and $m_{\rm s} = \pm 1$ can be driven by a resonant microwave magnetic field.

Figure 1(c) illustrates the experimental system, consisting of an optical module, a microwave driving module, a pulse control module, and a data analyzing module.

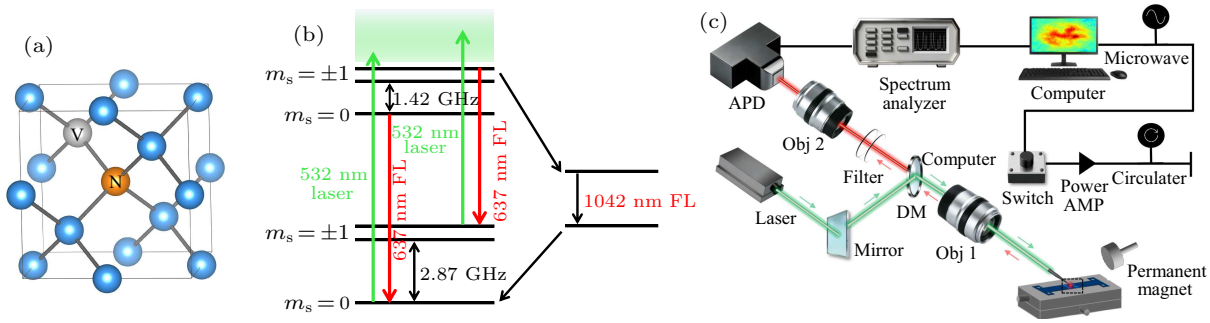


Fig. 1. (a) Structure of NV center; (b) energy levels diagram of NV center; (c) schematic of the experimental setup. The optical module is used for optical pumping and fluorescence readout of the NV center. The emitted red fluorescence is transmitted backward through the fiber, passes through the dichroic mirror and objective lens, and is detected by an avalanche photodiode (APD), which converts the optical signal into an electrical signal. The microwave driving module generates microwave magnetic fields resonating with the energy level transitions. The pulse control module enables alternating action between the laser and microwave, and introduces a subcarrier mechanism to improve the signal-to-noise ratio. The data analyzing module uses a motorized translation stage to scan the device under test, measuring the microwave magnetic field point by point under near-field conditions.[22]

3. Simulation design

Common rigid PCB materials (such as FR-4) lack conformability and have a certain thickness, failing to closely adhere to the surface of magnetic materials, posing challenges for microwave magnetic field imaging. In this work, we designed a splitting-combining flexible microwave device using a polyimide (PI) substrate, with a relative dielectric constant of 3.4, loss tangent $\tan\delta = 0.005$, and a substrate thickness h_1 of 0.1 mm. The design process of this device is shown in Fig. 2(a).

We started from the initial flat design, where the substrate is covered with conductive patches on the upper layer, and the lower copper layer serves as the device's reference ground. The thickness of copper h_2 is 0.018 mm. Through two 50 Ω impedance-characterized microstrip lines, the electromagnetic energy is concentrated in the inner ring area through the splitting-combining structure. To facilitate the extension of the tapered fiber, a through-hole is added. The edge of the hole is 0.1 mm away from the inner ring to prevent the drill from breaking the trace during processing. To ensure the transmission performance after conformal mapping, we chose to place the impedance matching part in the same plane. The radius of the sectoral short-circuited lines is then adjusted to fine-tune the operating frequency of the device to around 2.87 GHz. After rounding the corners, the energy loss during signal transmission is minimized. The key dimensions of the optimized device are shown in Table 1, and the related parameters are illustrated in Figs. 2(a) and 2(b). Figure 2(c) shows the design of a 3D-printed bracket with appropriate slots to hold the flexible device. The bottom of the bracket is equipped with holes for fixing the SMA connector. This design secures the device onto the bracket, forming an integrated probe, allow-

ing the fiber to be placed closer to the material under test, facilitating the subsequent scanning of magnetic materials. As shown in Figs. 2(d) and 2(e), simulated comparisons between the flat and conformal configurations show that bending introduces only limited variations in the S_{11} and S_{21} responses of the flexible device within the investigated frequency range of 2.6–3.1 GHz.

We found that as the radius of the middle ring decreases, the generated microwave magnetic field increases. By adjusting the inner radius r_3 of the ring, the operating frequency of the device can be tuned. Figure 2(f) shows the varied operating frequency of the device as r_3 changes. We further analyzed the dependence of the device bandwidth on other key structural parameters. The results show that, within the investigated range, the middle-ring size mainly affects the operating frequency, whereas its influence on the −10 dB bandwidth does not exhibit an obvious linear trend. By contrast, the radius of the sectoral short-circuited lines and the ring width have a more direct impact on the impedance-matching and coupling conditions, and therefore affect the effective bandwidth more significantly. The corresponding parametric results are shown in Figs. 2(g) and 2(h).

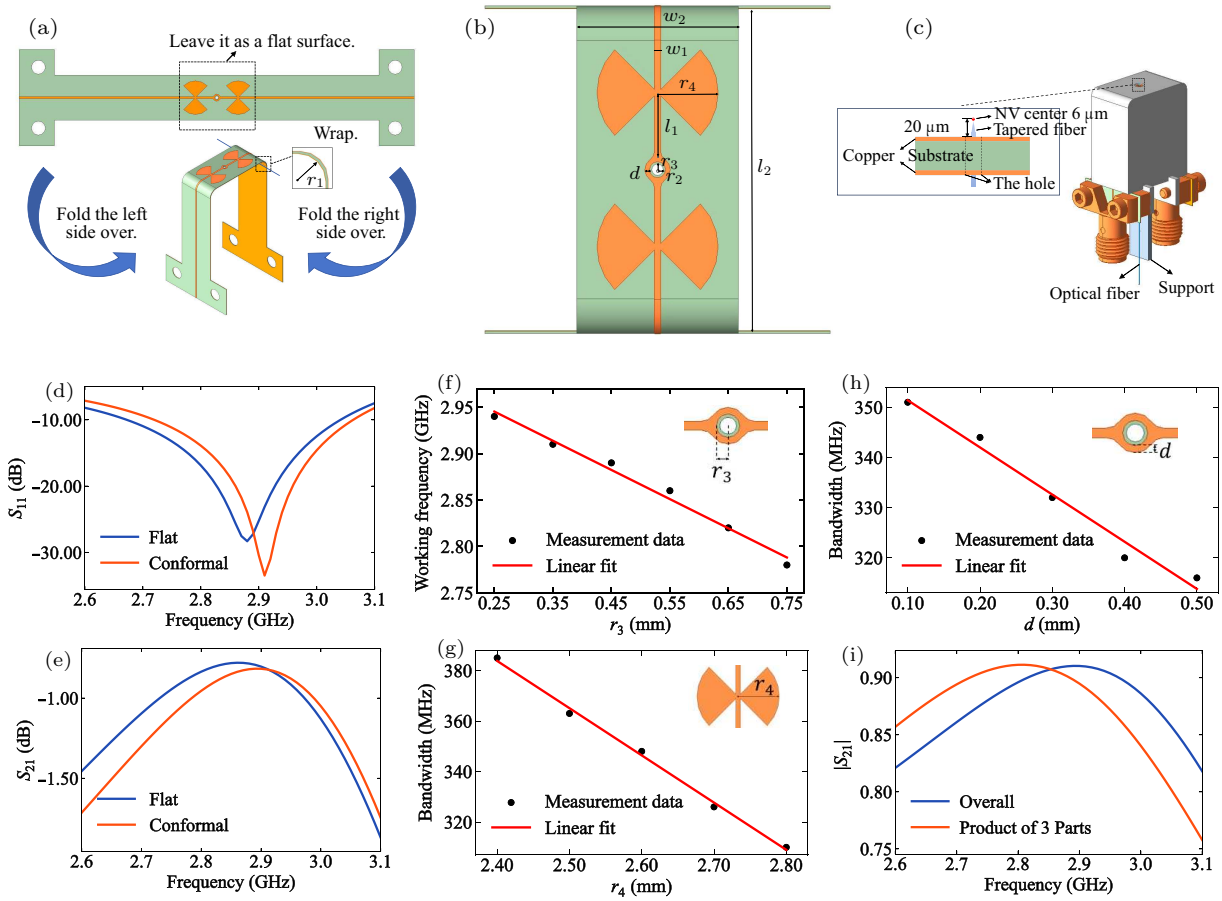


Fig. 2. (a) Planar structure of the device and conformal mapping diagram; (b) schematic of design parameters for the planar section after conformal mapping; (c) schematic of the integrated probe; (d) simulated S_{11} for the flat and conformal configurations; (e) simulated S_{21} for the flat and conformal configurations; (f) variation of the device operating frequency with r_3, showing an approximately linear dependence with a slope of about −0.3 GHz/mm; (g) dependence of the −10 dB bandwidth on the stub-line radius, showing an approximately linear dependence with a slope of about −187 MHz/mm; (h) dependence of the −10 dB bandwidth on the ring width, showing an approximately linear dependence with a slope of about −94 MHz/mm. (i) Comparison between the linear magnitude of $|S_{21}|$ for the overall structure and that reconstructed from the approximate cascade model.

Table 1. Main parameters of the conformal device.

Parameter	Description	Value (mm)
l_1	the length from the stub line to the inner circular ring	3
l_2	the length of the planar part of the device	14
w_1	the width of the microstrip feeder	0.27
w_2	the width of the middle part of the substrate	7
r_{cut}	the radius of the fillet at the corners of the ring shape	0.4
r_1	the radius of the fillet at the bend	1.5
r_2	the radius of the perforation within the ring	0.25
r_3	the inner radius of the ring	0.35
r_4	the radius of the stub line	2.63
d	the difference between inner and outer radius of the ring	0.2

As a two-port device, the flexible transmission line can be characterized by scattering parameters to describe its reflection and transmission properties, where S_{11} denotes the input reflection coefficient and S_{21} denotes the forward transmission coefficient.[23] To provide an intuitive description of how different structural sections contribute to the overall transmission behavior, we introduced an approximate cascade model based on the linear magnitude of S_{21}, so as to evaluate the consistency between the reconstructed cascade model and the overall structure, as shown in Fig. 2(i). This approximation was used only under the assumptions that multiple reflections at the interfaces are negligible and that impedance matching between adjacent sections is reasonably good.

Let $|S_{21}^{\mathrm{v}}(f)|$, $|S_{21}^{\mathrm{p}}(f)|$, and $|S_{21}^{\mathrm{all}}(f)|$ denote the linear magnitudes of the transmission coefficient for the vertical section, the planar section, and the overall structure, respectively, at frequency f. Since the combined structure can be approximately regarded as consisting of two vertical sections and one planar section connected in series, the reconstructed transmission magnitude $|S_{21}^{\mathrm{comp}}(f)|$ can be written as

$$\left|S_{21}^{\mathrm{comp}}(f)\right| = \left|S_{21}^{\mathrm{v}}(f)\right|^2 \cdot \left|S_{21}^{\mathrm{p}}(f)\right|. \tag{2}$$

To quantify the difference between the approximate cascade model and the overall structure, the relative error at frequency f is defined as

$$e(f) = \frac{|S_{21}^{\mathrm{comp}}(f) - S_{21}^{\mathrm{all}}(f)|}{|S_{21}^{\mathrm{all}}(f)|}. \tag{3}$$

Then in the 2.60–3.10 GHz, the calculated RMSRE is 0.04 between the approximate cascade model and the overall structure. The result indicates that conformal mapping introduces only a minor impact on the device transmission performance.

4. Experimental test of the conformal device

Figure 3(a) shows the processed flexible device, featuring microwave power input on one side and a 50 Ω end load on the other. The device's S_{11} was measured using a network analyzer. As shown in Fig. 3(b), from 2.6 GHz to 3.1 GHz, the simulation data align well with the measured data, with an actual bandwidth of 394 MHz when the input return loss is −10 dB. The operating frequency is approximately 2.87 GHz, with an S_{11} less than −30 dB. The measured value is −29.1 dB, indicating low return loss. This demonstrates the device's excellent impedance matching capability.

In addition, to provide a more complete experimental characterization of the device under conformal operation, we further measured and compared both S_{11} and S_{21} for the flat and conformal configurations. As shown in Figs. 3(c) and 3(d), only limited variations are observed in both the reflection and transmission responses under the investigated bending condition, indicating that conformal deformation does not significantly degrade the impedance matching or forward transmission capability of the device. Furthermore, we suppose that the discrepancy between simulation and measurement mainly originates from the difference between the practical RF connectors used in the experiment and the ideal wave-port excitation adopted in the simulation.

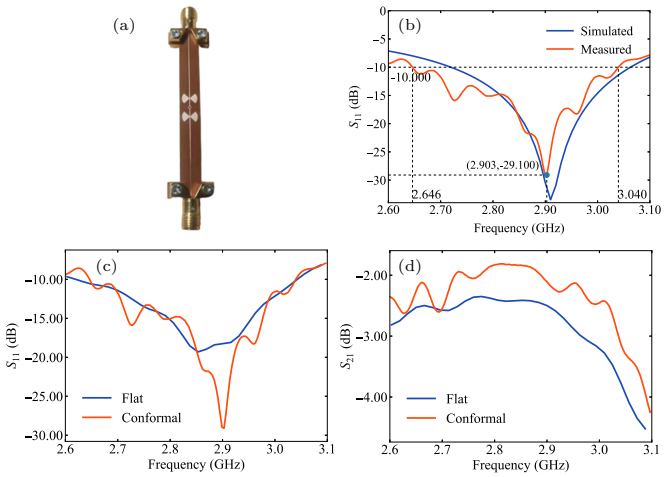


Fig. 3. (a) The processed flexible device. (b) Simulation and measurement data of S_{11}. The blue line represents simulation data, while the red line indicates network analyzer measurement data. (c) Measured S_{11} for the flat and conformal configurations. (d) Measured S_{21} for the flat and conformal configurations.

Under an applied static magnetic field, different projections of the field onto the four NV axes lead to eight resonance peaks in the ODMR spectrum, corresponding to the four NV orientations.[24–26] In the data analysis, each resonance peak was fitted individually using a single-Lorentzian function.[27] As shown in Fig. 4(a), the ODMR spectrum under a static magnetic field was obtained.

After the ODMR measurement, a typical Rabi oscillation experiment was performed at a position approximately 20 μm above this microwave device to determine the effective resonant microwave magnetic-field amplitude for the selected NV transition at 2.65 GHz, as shown in Fig. 4(b). This effective driving field, denoted as B_{mw}, can be calculated from the Rabi oscillation frequency according to

$$B_{\mathrm{mw}} = f/\gamma_{\mathrm{NV}}. \tag{4}$$

For the selected transition, the ground-state three-level system of the NV center $(m_{\mathrm{s}} = -1, 0, +1)$ is projected onto the effective two-level subspace $(m_{\mathrm{s}} = 0, +1)$ or $(m_{\mathrm{s}} = 0, -1)$. Therefore, the field B_{mw} extracted from the Rabi oscillation corresponds to the effective resonant driving field for the selected NV transition, rather than the total local microwave magnetic-field amplitude. For a locally linearly polarized microwave field, the effective circular driving component is smaller than the total field amplitude by a factor of $1/\sqrt{2}$.

Therefore, the actual local microwave magnetic-field amplitude satisfies $B = \sqrt{2}B_{\mathrm{mw}}$

Since the frequency of the fitted curve in Fig. 4(b) is 2.93 MHz, the corresponding actual microwave magnetic field amplitude is 1.48 Gauss (B). We use the microwave efficiency Λ to quantify the device's ability to convert excitation power into a microwave magnetic field, as expressed in formula[28]

$$\Lambda = \frac{B}{\sqrt{P}}. \tag{5}$$

Here, P represents the actual microwave power delivered to the device input after correcting for the insertion loss of the microwave delivery path, including the cable and connectors.

With an experimentally measured excitation power of 20.08 dBm, the microwave efficiency at this point is calculated to be 4.64 $\mathrm{G}/\sqrt{\mathrm{W}}$. For ensemble NV centers, a sufficiently high microwave efficiency is generally required to achieve effective microwave driving. The microwave efficiency obtained in this work is adequate for the subsequent experimental measurements.

A complete Rabi oscillation curve consumes time. When the microwave pulse duration is extremely short, the Rabi oscillation curve approximates a linear function.[29] Therefore, as shown in Fig. 4(b), the corresponding fluorescence intensity can be measured and the microwave magnetic field distribution of the device can be rapidly scanned.

To determine the optimal position for the optical fiber, a meticulous scan of the planar area with a radius of 250 μm was conducted approximately 20 μm above the microwave transmission line. We used the first selected resonance peak in Fig. 4(a) for analysis. This scan was performed under precise control of the LABVIEW software, employing a step size of 10 μm. Figure 4(c) shows the simulated surface normalized distribution of the microwave magnetic field, while Fig. 4(d) shows the experimentally measured normalized distribution near 2.87 GHz. For quantitative comparison, the similarity between the two distributions was evaluated using the Pearson correlation coefficient. The calculated correlation coefficient is 0.86, indicating good consistency in the overall spatial distribution trends. Although discrepancies in magnitude remain, the correlation analysis shows that the experimental results capture the main spatial features of the simulated distribution.

Furthermore, we investigated axial attenuation using a displacement stage. With the diamond probe positioned approximately 100 μm from the borehole edge, we performed longitudinal scans at 10 μm intervals, starting approximately 20 μm above the microwave transmission line, as shown in Fig. 4(e). The measured and simulated data points were normalized respectively. To quantitatively evaluate the agreement between the measured data points and the simulated curve, RMSE between the normalized measured data and the normalized simulated values at the same sampling positions was calculated. The resulting RMSE is 0.05, indicating a generally consistent trend between the simulated and measured axial attenuation profiles.

Moreover, the magnetic field at 100 μm from the edge of the scanning plane exceeded 1 Gauss, sufficient to excite the NV center. Therefore, we coupled the optical fiber to the NV center, which is encapsulated within a device and support structure, as shown in Fig. 2(c).

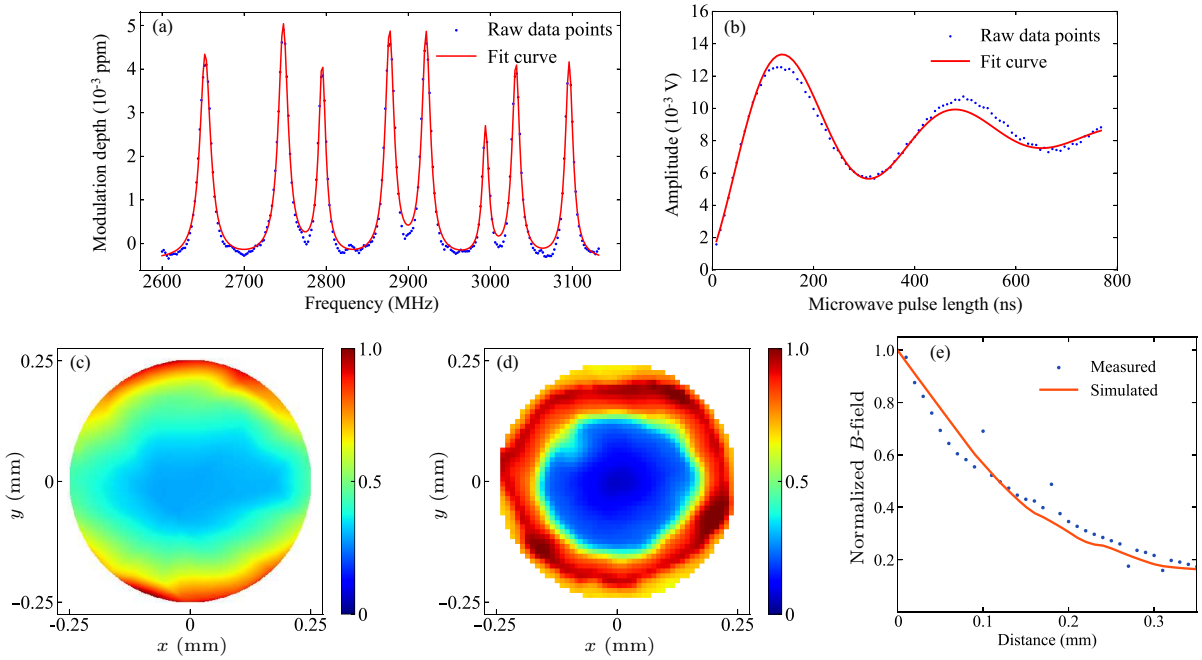


Fig. 4. (a) ODMR spectrum of the nitrogen-vacancy center under an applied static magnetic field; (b) measured Rabi oscillation data and fitted curve; (c) simulated surface microwave magnetic field normalized distribution; (d) measured surface microwave magnetic field normalized distribution; (e) variation with axial distance at a position 100 μm away from the aperture edge.

In order to more effectively verify its application value in the characterization of magnetic materials, we used the integrated probe shown in Fig. 2(c) to conduct a two-dimensional characterization on the surface of kagome magnet $TmMn_6Sn_6$, which is a representative micro-magnetic material.[30] Based on reasonable inference, the selected scanning area was approximately located at 50 μm above the surface of the micro-magnetic material, as shown in Fig. 5(a). The optical image of the sample is shown in Fig. 5(b), using a Mitutoyo long-working-distance objective with far-field correction. The applied bias magnetic field was approximately 200 Gauss, the scanning area size was 500 μm × 500 μm, and the scanning step size was 9.375 μm.

Under the applied bias magnetic field, the resonance frequencies of the selected ODMR doublet shift with the local static magnetic field. At each scanning point, we first fitted the ODMR spectrum and selected one pair of resonance peaks belonging to the same NV axis, whose center frequencies were denoted as f_u and f_l ($f_u > f_l$). These two fitted center frequencies were then used to reconstruct the local static magnetic-field magnitude B and the angle θ between the local magnetic field and the selected NV axis.

Specifically, the magnetic field magnitude B is given by[31]

$$B = \frac{1}{\sqrt{3}}\sqrt{f_u^2 - f_u f_l + f_l^2 - D^2 - 3E^2}. \tag{6}$$

And the angle θ is obtained from[31]

$$\cos^2\theta = \frac{-f_u^3 - f_l^3 + 3f_u^2 f_l - 3f_u f_l^2}{27B^2(D-E)} + \frac{D}{3(D-E)} - \frac{2DE^2}{3B^2(D-E)} - \frac{E}{D-E} + \frac{2D^3}{27B^2(D-E)}. \tag{7}$$

In this work, the parameters D and E were determined from the zero-field ODMR spectrum and treated as fixed during the scan. The external magnetic field was aligned approximately along the vertical direction. The selected pair of peaks corresponds to the outermost resonance pair, which indicates that the projection of the magnetic field onto the corresponding NV axis is the largest. Therefore, this NV axis is the closest to the direction of the applied magnetic field.

The resulting spatial distribution of the static magnetic-field magnitude is shown in Fig. 5(c), reflecting the spatial variation of the magnetic-field distribution on the sample surface. Correspondingly, the spatial distribution of θ is shown in Fig. 5(d). The relatively larger θ values in the lower-right region indicate that the local static magnetic field there has a stronger transverse component with respect to the selected NV axis. These results demonstrate that the fiber–diamond integrated probe can be used for static magnetic-field characterization of micro-magnetic materials.

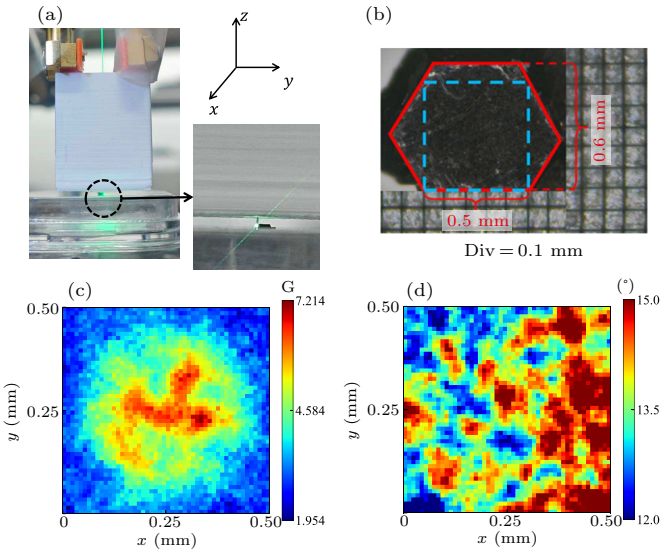


Fig. 5. (a) Experimental site diagram; (b) optical image of the micro-magnetic material. The red outline indicates the actual size and contour of the magnetic material, and the blue dashed box marks the actual scanning area. Each small grid division corresponds to 0.1 mm. (c) Spatial distribution of the static magnetic-field amplitude B within a 500 μm × 500 μm scanning area on the sample surface. (d) Spatial distribution of the angle θ between the static magnetic field and the selected NV axis.

5. Conclusion and perspectives

This paper designs and implements a flexible microwave transmission structure suitable for diamond NV center quantum sensing. This structure balances efficient microwave magnetic field and broadband, with a bandwidth of 394 MHz and a microwave efficiency of 4.64 G/$\sqrt{\text{W}}$. Furthermore, this microwave structure is integrated with a fiber-diamond probe.

A scanning plane with a radius of 250 μm was established approximately 20 μm above the transmission line, and the microwave magnetic field distribution was measured. Simultaneously, the microwave magnetic field remained above 1 G at approximately 100 μm from the aperture edge, verifying the attenuation law of the microwave magnetic field in the axial direction, thus determining the appropriate placement of the fiber. Two-dimensional scanning characterization of the local static magnetic field on the surface of the magnetic sample was also performed.

Future research could further optimize flexible structures to improve the local microwave magnetic field strength and spatial uniformity, and combine them with smaller diamond sensing units and high-precision scanning systems to enhance magnetic-field imaging capability.

Acknowledgement

We acknowledge financial support by the Jiangsu Science and Technology Major Project (Grant No. BG2025017).

References

[1] Glenn D R, Bucher D B, Lee J, Lukin M D, Park H and Walsworth R L 2018 *Nature* **555** 351

[2] Kim S, London P, Yang D P, Hughes L B, Ahlers J, Meynell S, Mitchell W J, Mukherjee K and Bleszynski Jayich A C 2025 *Nat. Commun.* **16** 9803

[3] Mariani G, Nomoto S, Kashiwaya S and Nomura S 2020 *Sci. Rep.* **10** 4813

[4] Huang K, Mao X B, Zhang Y, Wang M Z, He X H, Ran G H, Hu Q and Lin Z N 2024 *IEEE Trans. Instrum. Meas.* **73** 9518009

[5] Taylor J M, Cappellaro P, Childress L, Jiang L, Budker D, Hemmer P R, Yacoby A, Walsworth R and Lukin M D 2008 *Nat. Phys.* **4** 810

[6] Yang Y, Wu Q, Wang Y P, Chen W H, Yu Z F, Yang X F, Fan J W and Chen B 2023 *Opt. Continuum* **2** 1426

[7] Yaroshenko V, Soshenko V, Vorobyov V, Bolshedvorskii S, Nenasheva E, Kotel'nikov I, Akimov A and Kapitanova P 2020 *Rev. Sci. Instrum.* **91** 035003

[8] Zhao M, Lin Q J, Zhu L Q, Zhao L B and Jiang Z D 2020 *Micro Nano Lett.* **15** 793

[9] Xie T T, Gong P W, Xie W, Chai J, Jiang H and Liu J C 2025 *Sci. Rep.* **15** 13152

[10] Bayat K, Choy J, Baroughi M F, Meesala S and Loncar M 2014 *Nano Lett.* **14** 1208

[11] Babashah H, Losero E and Galland C 2024 *Open Res. Eur.* **4** 44

[12] Xia S K, Lu W T, Zhao X T, Xue Y W, Xu Z B, Ge S Y, Wang Y, Yu L Y, Bian Y C, An S H, Yang B, Xiang J J and Du G X 2024 *Chin. Phys. B* **33** 054202

[13] Eisenach E R, Barry J F, Pham L M, Rojas R G, Englund D R and Braje D A 2018 *Rev. Sci. Instrum.* **89** 094705

[14] Dolde F, Fedder H, Doherty M W, Nöbauer T, Rempp F, Balasubramanian G, Wolf T, Reinhard F, Hollenberg L C L, Jelezko F and Wrachtrup J 2011 *Nat. Phys.* **7** 459

[15] Le X P, Mayer L, Magaletti S, Schmidt M, Roch J F and Debuisschert T 2025 *Commun. Eng.* **4** 209

[16] Schwade M, Zhang S, Vonhoff F, Delgado F P and Egger D A 2026 *Nat. Commun.* **17** 2652

[17] Lu W T, Xia S K, Chen A Q, He K H, Xu Z B, Chen Y H, Wang Y, Ge S Y, An S H, Wu J F, Ma Y H and Du G X 2024 *Chin. Phys. B* **33** 080305

[18] Lu W T and Du G X 2025 *IEEE United Conf. Millim. Waves Terahertz Technol.* 1

[19] Ye Q Y, Xue Y W, He F Y, Zhao X T, Bian Y C, Lu W T, Wang J X, Chen H H, Xia S K, Zeng M J and Du G X 2024 *Chin. Phys. B* **33** 024202

[20] Herrmann J, Appleton M A, Sasaki K, Monnai Y, Teraji T, Itoh K M and Abe E 2016 *Appl. Phys. Lett.* **109** 183111

[21] Fischer J, Herrmann Y, Wolfs C F J, Scheijen S, Ruf M and Hanson R 2025 *Nat. Commun.* **16** 11680

[22] Shi K Q, Hang H, Lu W T, Huang J C, Li N, Wang J X, Xu Z B, Yu L Y, Xia S K, Bian Y C and Du G X 2025 *Chin. Phys. B* **34** 094205

[23] Hong C, Li Z Q, Guan W and Liang L P 2025 *Sci. Rep.* **15** 23096

[24] He W H, Dong M M, Hu Z Z, Zhang Q H, Yang B, Liu Y, Fan X L and Du G X 2019 *Chin. Phys. Lett.* **36** 127601

[25] Guo Y Z, Coccia G, Kavatamane V K, Giakoumaki A N, Vetlugin A N, Ramponi R, Soci C, Barclay P E, Hadden J P, Bennett A J and Eaton S M 2025 *Nano Lett.* **25** 8096

[26] Duan D W, Kavatamane V K, Arumugam S R, Rahane G, Tzeng Y K, Chang H C, Sumiya H, Onoda S, Isoya J and Balasubramanian G 2018 *Appl. Phys. Lett.* **113** 041107

[27] Zhao X T, He F Y, Xue Y W, Ma W H, Yin X H, Xia S K, Zeng M J and Du G X 2024 *Chin. Phys. B* **33** 048502

[28] Jia W F, Shi Z F, Qin X, Rong X and Du J F 2018 *Rev. Sci. Instrum.* **89** 064705

[29] Dong M M, Hu Z Z, Liu Y, Yang B, Wang Y J and Du G X 2018 *Appl. Phys. Lett.* **113** 131105

[30] Wang B, Yi E K, Li L Y, Qin J W, Hu B F, Shen B and Wang M 2022 *Phys. Rev. B* **106** 125107

[31] An S H, Ge S Y, Lu W T, Chen G B, Xia S K, Chen A Q, Wang C K, Yu L Y, Zhang Z Q, Wang Y, Tang G J, Cheng H F and Du G X 2024 *Chin. Phys. B* **33** 120305